Light-scattering measurements of monomer size, monomers per aggregate, and fractal dimension for soot aggregates in flames

C. M. Sorensen, J. Cai, and N. Lu

A new method for the *in situ* optical determination of the soot-cluster monomer particle radius a, the number of monomers per cluster N, and the fractal dimension D is presented. The method makes use of a comparison of the volume-equivalent sphere radius determined from scattering–extinction measurements R_{SE} and the radius of gyration R_g, which is determined from the optical structure factor. The combination of these data with the measured turbidity permits for a novel measurement of D. The parameters a and N are obtained from a graphical network-analysis scheme that compares R_{SE} and R_g. Corrections for cluster polydispersity are presented. The effects of uncertainty in various input parameters and assumptions are discussed. The method is illustrated by an application to data obtained from a premixed methane–oxygen flame, and reasonable values of a, N, and D are obtained.

Key words: Optical particle sizing, soot, fractals.

1. Introduction

In situ optical techniques for particle sizing are highly desirable because of their inherently nonperturbative nature and their ability to provide remote sensing in hostile environments. Because of this desirability, the development and application of these techniques have seen considerable effort in the past, especially with regard to combustion-generated soot aerosols.[1–8] Despite these efforts, however, the amount of information regarding the details of the structure of particle clusters obtainable through optical techniques is significantly lacking compared with the straightforward concept of collection and visual examination with an electron microscope. The inability to quantitatively describe the typical random chainlike nature of particle clusters severely hampered these early efforts. This inability has lessened in the last decade, however, with the development of the fractal concept, which has been shown to describe accurately soot aggregates collected from flames.[9–14] Recently, both theoretical[15–18] and experimental[19–21] research has appeared to understand light scattering from soot fractal aggregates and thus to use light scattering to measure the mean size and fractal dimension. Opportunity exists to improve these measurements as well as to more fully use this new fractal description.

It is the purpose of this paper to do the latter. We will show how comparison of the well-established scattering–extinction measurement of the mean size to the cluster radius of gyration, which is determined by the dependence of the scattered intensity on the scattering angle, can yield the cluster fractal dimension D, the mean radius of its monomers a, and the mean number of monomers per cluster N. This method works because the scattering–extinction radius R_{SE} depends on the total volume of soot material per cluster, whereas the radius of gyration R_g depends both on this and the fractal dimension. Given an independent relation among material, radius, and fractal dimension, which are obtained from either computer simulations or analytic arguments, one can obtain the three parameters a, N, and D. Our method of analysis is graphical. On a graph of R_{SE} versus R_g, a network of lines of constant a and N can be plotted from the theory. When plotted on this network, data for R_{SE} and R_g indicate the values of a and N.

In the following sections we describe the current state of knowledge of fractal optics relevant to light scattering. From this knowledge we theoretically show how our method for determining D, a, and N should work and describe our graphical network-analysis scheme. We then describe experiments on a

The authors are with the Department of Physics, Kansas State University, Manhattan, Kansas 66506-2601.

Received 04 November 1991.
0003-6935/92/306547-11$05.00/0.

premixed methane–oxygen flame to measure R_{SE}, R_g, and the turbidity τ. With these quantities we use our graphical analysis to measure D, a, and N, the latter two as a function of height above the burner, in our flames. Reasonable values with reasonable uncertainties are obtained. We then discuss the effects and consequences of relaxing various assumptions, most notably the effect of cluster polydispersity on our measured values of a and N. We also briefly describe the propagation of uncertainty in some of our input parameters on the three values measured.

2. Optics of Fractal Aggregates

A. General

Forrest and Witten[9] first showed that cluster aggregates have a fractal morphology with a quantitative fractal dimension. Since then, numerous studies have shown that the fractal morphology is a universal consequence of aggregation.[10,11] A fractal may be defined as an object with scale-invariant symmetry, i.e., it looks the same on a variety of length scales.[12] For clusters, a consequence of this scale invariance is that the number of monomer units N in a cluster scales with the cluster radius of gyration R_g as

$$N \sim R_g^{D}, \tag{1}$$

where D is a noninteger fractal dimension. Another consequence of the scale invariance is a power-law density-autocorrelation function. The Fourier transform of this quantity is the structure factor $S(\hat{q})$ for scattered radiation, and it too is a power law of the form[15–17]

$$S(q) \sim q^{-D}, \tag{2}$$

where q is the scattered wave vector, $q = 4\pi\lambda^{-1} \sin \theta/2$. This result is obtained under the approximation that multiple scattering within the aggregate is small,[18] which is a good approximation for soot when the monomer size is small. Relation (2) is the optical signature of a fractal and is the usual way the fractal dimension is determined. This relation holds for $qR_g > 1$, but $S(q)$ is constant for $qR_g < 1$ and this crossover can be used to determine R_g.[21] Because length scales in typical colloidal or aerocolloidal clusters range from $\sim$10 nm for the monomer size to a few hundred nanometers for the cluster size, an appropriate radiation to make structure-factor measurements on fractal aggregates is light.

B. Light Scattering and Absorption

For light scattering and absorption, here we give a theoretical review of the optical properties of fractal aggregates[15–18] such as soot particles. Soot monomers or primary particles are small essentially spherical bodies with a complex index of refraction m and a radius of $a \ll \lambda$. We consider a scattering geometry with a horizontal scattering plane and vertically polarized incident light. The Rayleigh theory for small particles gives for the monomer-polarized absorption and differential scattering cross sections[22]

$$\sigma_{\text{abs}}^{\text{mon}} = 4\pi k a^3 E(m), \tag{3}$$

$$\frac{d\sigma_s^{\text{mon}}}{d\Omega} = k^4 a^6 F(m), \tag{4}$$

where $k = 2\pi/\lambda$ is the incident wave vector and

$$E(m) = -\text{Imag}\left(\frac{m^2 - 1}{m^2 + 2}\right), \tag{5}$$

$$F(m) = \left|\frac{m^2 - 1}{m^2 + 2}\right|^2. \tag{6}$$

For fractal clusters of N monomers per cluster and a fractal dimension less than 2, it is predicted that[15,17]

$$\sigma_{\text{abs}}^{c} = N\sigma_{\text{abs}}^{\text{mon}} = 4\pi N k a^3 E, \tag{7}$$

$$\frac{d\sigma_s^c(q)}{d\Omega} = N^2 S(x) \frac{d\sigma_s^{\text{mon}}}{d\Omega} = k^4 a^6 F N^2 S(x). \tag{8}$$

In Eq. (8) we include the possible functional dependence of the differential cross section on the scattering wave vector

$$q = 2k \sin \theta/2 = 4\pi\lambda^{-1} \sin \theta/2, \tag{9}$$

where θ is the scattering angle. This angle enters through the optical structure factor $S(x)$ with $x = qR_g$, where R_g is the radius of the gyration of the cluster. We see that $S(x)$ has the limits $S(x) = 1$ for $x \ll 1$ and $S(x) = x^{-D}$ for $x \gg 1$ where D is the fractal dimension.

C. Scattering–Extinction Measurements

In a scattering–extinction measurement, one measures both the scattered light at a given angle and the extinction of the incident beam.[1,2] Such a measurement is most effective at a scattering angle θ such that $x = qR_g \ll 1$, then $S(x) = 1$. For the sake of clarity we will assume the cluster distribution is monodisperse, i.e., they all have the same N. Later we shall describe changes that must be made for the polydisperse case. The scattered power at the detector is

$$P_s = I_0 c k^4 a^6 F N^2 n. \tag{10}$$

In Eq. (10) I_0 is the incident intensity, n is the cluster number density and c is a calibration constant. This constant can be determined by the scattering from gases of known optical cross sections under an identical scattering geometry.

The extinction or turbidity is measured by comparing the light incident on and transmitted through the flame

$$I_T = I_0 \exp(-\tau l), \tag{11}$$

where l is the beam pathlength in the flame. The turbidity, or extinction, should be a result of both

absorption and scattering,

$$\tau = n\sigma_{abs}{}^{c} + n\sigma_{scat}{}^{c}, \tag{12}$$

where $\sigma_{scat}{}^{c}$ is the total scattering cross section for the cluster. For small particles of complex m, $\sigma_{abs}{}^{c} \sim Na^3$, whereas $\sigma_{scat}{}^{c} \sim N^2a^6$, hence one may often use the approximation

$$\tau = n\sigma_{abs}{}^{c} = n4\pi Nka^3E \tag{13}$$

with reasonable accuracy.

With these measurements a radius, which we will call the scattering–extinction radius R_{SE}, and number density can be found as

$$R_{SE}{}^3 = a^3N = \frac{4\pi E}{Fk^3}\frac{P_s/I_0c}{\tau} \tag{14}$$

$$n = \frac{k^2F}{E^2}\frac{\tau^2}{P_s/I_0c}. \tag{15}$$

The measurable quantities are P_s/I_0c and τ, k is determined by the incident light, and E and F must be calculated from a somewhat poorly determined index of refraction, m. Equations (14) and (15) reproduce the way scattering–extinction has been analyzed for the past 20 years,[1,2] and we see the important fact that the R_{SE} is a volume-equivalent sphere radius, $aN^{1/3}$.

D. R_g Measurement

Optical structure-factor measurements permit a more realistic determination of the cluster radius through the radius of gyration R_g. Obviously, R_{SE} does not change as a cluster of a given N goes from compact to the more factual ramified size, but R_g does change and accurately quantifies the ramified cluster size. Furthermore, R_g is determined without the need to know the often poorly known particle index of refraction. Hence, by some standards, R_g is a better parameter than R_{SE} for size description. Recalling Eq. (8), we may write for the light-scattering intensity from an ensemble of clusters at wave vector q

$$I(q) = I(0)S(qR_g). \tag{16}$$

The exact form of $S(x)$ is dependent on the morphology. For $qR_g \lesssim 1$, which is the so-called Guinier regime, this dependence is well described by

$$I(q) = I(0)(1 - \tfrac{1}{3}q^2R_g{}^2) \tag{17}$$

for any morphology. Thus a plot of $I(0)/I(q)$ versus q^2 is linear with slope $R_g{}^2/3$. We have demonstrated this in previous research to determine R_g in CH_4/O_2 premixed flames.[21]

E. Comparison of Methods

In a comparison of the methods, the scattering–extinction and R_g measurements yield different types of information regarding the same particle clusters: the total amount of substance in the cluster from S/E and the ramified size from R_g. Thus if we have a connection relating substance to size, a combination of the two methods will yield more information. The relation we need is between N and R_g and it is

$$N = k_0(R_g/a)^D, \tag{18}$$

where k_0 is a constant for a given D.

We now combine Eqs. (14) and (18) to find

$$R_{SE} = k_0{}^{1/3}a^{1-D/3}R_g{}^{D/3}. \tag{19}$$

Equation (19) shows that log–log graphs of experimental values of R_{SE} versus R_g should be linear with slope $D/3$ and the position of the line (i.e., the intercept) dependent on a. Further manipulation to eliminate a in favor of N in Eq. (19) by using Eq. (18) yields

$$R_{SE} = k_0{}^{1/D}N^{1/3-1/D}R_g. \tag{20}$$

Equation (20) shows the lines of constant N on a log–log graph of R_{SE} versus R_g would have a unity slope.

Equations (19) and (20) suggest the following scheme for determination of a and N: A log–log graph is made of R_{SE} versus R_g. Lines of constant a would have slope $D/3$ with different a values parallel to each other. Lines of constant N would cross these lines and have a slope of 1. Thus a network of lines would result. Experimental data plotted on such a graph would yield both a and N. To make this scheme work we need two more quantities—the value of k_0 and the value of D.

1. *Value of k_0*

The constant k_0 of Eq. (18) can be determined from the data of computer simulations or from calculations involving the $N \to 1$ limit. From a calculational point of view and lacking a more quantifiable alternative, we expect Eq. (18) to have the correct $N = 1$ limit. When $N = 1$, only the spherical monomer is present. The radius of gyration for a sphere is $R_g = (3/5)^{1/2}a$. Thus $N = 1$ implies $1 = k_0[(3/5)^{1/2}a/a]^D$ and hence

$$k_0 = (5/3)^{D/2}. \tag{21}$$

In their simulations Mountain and Mulholland[16] created an ensemble of particles for which a best fit to Eq. (18) yielded $k_0 = 1.55$ and $D = 1.90$. For $D = 1.90$, Eq. (21) predicts $k_0 = 1.62$ in excellent agreement with this simulation. In another simulation Mulholland et al.[23] found $D = 1.91$ and $k_0 = 1.30$ whereas Eq. (21) predicts $k_0 = 1.63$, which is only a fair agreement.

2. *Determination of D*

To the best of our knowledge, to date the method to determine the fractal dimension D by optical means has been the power-law form of the structure factor at large qR_g, $S(qR_g) \sim (qR_g)^{-D}$. Given such a measurement, we are ready to apply the proposed

scheme for the determination of a and N. This measurement is not always feasible, however, given the limited range of q available in optics experiments. Indeed, both Hurd and Flower[19] and earlier work from this laboratory[21] found that qR_g was limited to $\lesssim 5$ in flame systems and that D was not determined with good precision.

Equation (19) suggests an alternative means to determine D if the monomer size is constant. This constancy is usually not the case in sooting flames, as surface growth continues throughout the flame after the initial burst of nucleation.[1,24,25] It is well known that this surface growth can be monitored by measuring the total volume fraction of the soot through a turbidity measurement. If we make a crucial yet well-justified assumption that the total number of monomers in the flame is determined in the reaction zone during nucleation and is constant thereafter, then further change in the volume fraction occurs only through a change in the monomer radius a. Equation (13) for the turbidity shows that if the total number of monomers N is constant, τ will monitor the change in a. The change in a relative to some reference point in the flame can be obtained by ratioing Eq. (13), $\tau/\tau_0 = (a/a_0)^3$, where the subscript zero designates the reference point. Ratioing Eq. (19) eliminates the k_0, and the resulting ratio of a can be eliminated for τ and after some rearrangement leads to

$$\frac{R_{SE}}{R_{SE,0}}\left(\frac{\tau_0}{\tau}\right)^{1/3} = \left[\frac{R_g}{R_{g,0}}\left(\frac{\tau_0}{\tau}\right)^{1/3}\right]^{D/3}. \tag{22}$$

To use Eq. (22) we measure a series of R_{SE}, R_g, and τ values at various positions in the flame. One position is then chosen as the reference position. The left- and right-hand (without the $D/3$ power) sides of Eq. (22) are then calculated and graphed against each other on a log–log plot. The slope should be $D/3$, independent of a, N, and k_0.

In Section 3 we will describe our measurements of R_{SE}, R_g, and τ. A graph using Eq. (22) will be made and D will be determined. Then a graph of R_{SE} versus R_g will be made using this value of D. From this second graph values of a and N will be extracted by means of the network of lines suggested by Eqs. (19) and (20).

3. Experimental Method

Our experimental apparatus was the same as that used previously in the literature.[21] Our flame was supported on a cooled porous frit burner obtained from McKenna Products. The premixed gases passed through a 6-cm-diameter frit. This frit was surrounded by an annular sheath region 0.5 cm wide through which nitrogen was passed. A 15-cm-diameter steel stagnation plate was placed 30 mm above the burner surface to stabilize the flame.

The gases used were methane and oxygen that were premixed before the burner. Their flows were controlled by critical orifices that we calibrated with a dry-test flowmeter. The cold gas velocity of the mixture, uniform across the frit, was 6 cm/s. The nitrogen sheath flow was also controlled by critical orifices to a velocity of 5 cm/s. This arrangement yielded a quasi-one-dimensional flame with the only major variable being the height above the burner, h. The fuel-to-oxidizer ratio of these flames is described by the ratio of carbon atoms to oxygen atoms, C/O, in the gas mixture. We used two ratios, C/O = 0.69 and C/O = 0.75. The C/O ratio for complete combustion to H_2O and CO_2 is 0.25.

The flatness of the flame, i.e., the uniformity across a given diameter, was checked as described previously in the literature.[21] The flame was flat, so all the soot in the scattering volume had the same optical properties.

Our light-scattering apparatus used an argon–ion laser operating at $\lambda = 488$ nm as a source. The vertically polarized light was focused by a 50-cm focal-length lens into the flame. The burner was mounted on a x-y-z-translation stage over the pivot of our goniometer. This was an optical rail 1 m long. This rail rotated about the pivot on a flat optical table. A careful alignment of the goniometer was made to ensure that the center of the scattering volume did not move as the angle was changed. Mounted on the rail was a 10-cm focal-length collection lens that imaged the incident beam onto an iris diaphragm with unity magnification, which gave us a scattering volume 1 mm long at 90°. Light passing through this iris diaphragm then passed through a 488-nm notch filter to eliminate the blackbody light from the hot soot. Detection was made with an ITT FW130 photomultiplier tube. Its analog output was converted to a digital signal, which was read by a PC. Values of the scattered light were sampled once per second with 1-s integration times. The variation between samples was usually less than 1%.

The incident and transmitted intensities of the laser beam necessary for the turbidity measurements were measured with an RCA 1P28 photomultiplier tube, which intercepted the beam after it passed through over the burner.

A typical run started with the calibration of the scattering volume at $\theta = 20°$ with gases with a known Rayleigh ratio. The gases we used were N_2, O_2, and C_2H_4. Graphs of $I(20°)$ versus the gas Rayleigh ratio were linear and intercepted the origin within experimental error. Slopes of these graphs yielded the calibration constant c.

The flame was then ignited and allowed to stabilize for a few minutes. The stagnation plate was cleaned of built-up soot before a given run. The lowest height, $h = 10$ mm, was selected and the intensity as a function of θ was measured sequentially from 10° to 110°. This process took approximately 1.5 min. The values of the intensity were corrected for the change in scattering volume as θ varied by multiplying by $\sin\theta$ to yield $I(q)$. Higher heights were then measured after the occasional cleaning of the stagna-

tion plate. Repeating lower heights at later times showed good reproducibility to 3%.

4. Data Analysis

As suggested by Eq. (17), R_g was determined by plotting $I(q)^{-1}$ versus q^2. The linearity of such graphs was quite good, as we found previously.[21] Linear least-squares fits to these plots yield the intercept $[I(0)^{-1}]$ and the slope $(R_g^2/3)$. Values for R_g versus h for both flames are shown in Fig. 1. These values are in reasonable agreement with our earlier results.[21]

The scattering–extinction radius R_{SE} was determined by using Eq. (14) with our measured c and P_s equal to the value of the scattered intensity at $\theta = 20°$, which is well in the $qR_g \ll 1$ regime. Values of $E = 0.26$ and $F = 0.22$ determined from the Dalzell–Sarofim index of refraction,[26] $m = 1.56 - 0.56i$, were used. Values of R_{SE} versus h are also graphed in Fig. 1. One readily sees $R_{SE} < R_g$ at all h, as we expected from the physical meaning of these two quantities discussed in Section 2.

We now apply Eq. (22) to determine the fractal dimension D from our measured values of R_g, R_{SE}, and τ. Our reference position is $h = 10$ mm. Figures 2 and 3 display our results for the C/O = 0.69 and C/O = 0.75 flames, respectively. The linearity of these graphs is quite good, and fits to the slope yield values of $D = 1.75$ and $D = 1.70$ for C/O = 0.69 and C/O = 0.75, respectively. These values are in good agreement with each other and with theoretical expectations from numerous simulations of diffusion-limited aggregation[10,11,16] and earlier experimental results on flame-generated aerosols.[13,14,19,20]

Given D, we are now ready to apply Eqs. (19) and (20) to determine a and N. We use an average from both flames of $D = 1.73$. Hence $k_0 = 1.56$. Logarithmic graphs of R_{SE} versus R_g are given in Figs. 4 and 5 for C/O = 0.69 and C/O = 0.75, respectively. These graphs include our network of constant a and constant N lines. Errors of precision and accuracy are also included in Figs. 4 and 5. The filled circles represent the precision of our measurements of R_g and R_{SE} determined from run-to-run reproducibility. This precision is ±2% for each R. We have also included an accuracy estimate in the form of an error bar for R_{SE}. This estimate was determined from uncertainties in the turbidity. This error is bigger than the precision.

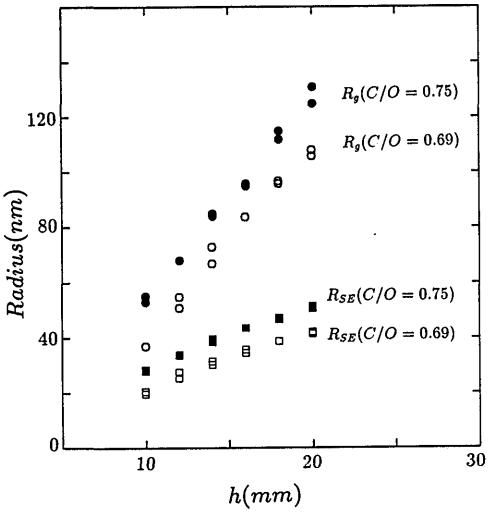

Fig. 1. Radius of gyration R_g or scattering–extinction radius R_{SE} as a function of the height above burner for two different flames. Two runs are shown to demonstrate the reproducibility of the data.

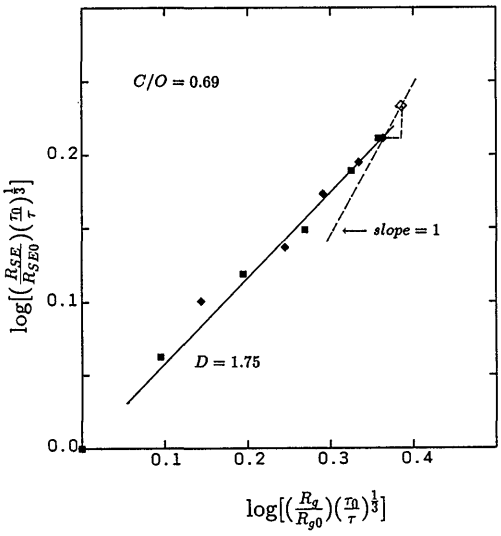

Fig. 2. Plot of the data in accordance with Eq. (22) for the C/O = 0.69 flame. Two runs are shown to demonstrate reproducibility. The slope of this graph is $D/3$ to imply $D = 1.75 \pm 0.10$. The open diamond represents the correction of the closed diamond that joins it on the dashed line, which accounts for the variation in flame temperature with the height above burner. The dashed line of slope = 1 is where the correction would occur for any temperature variation.

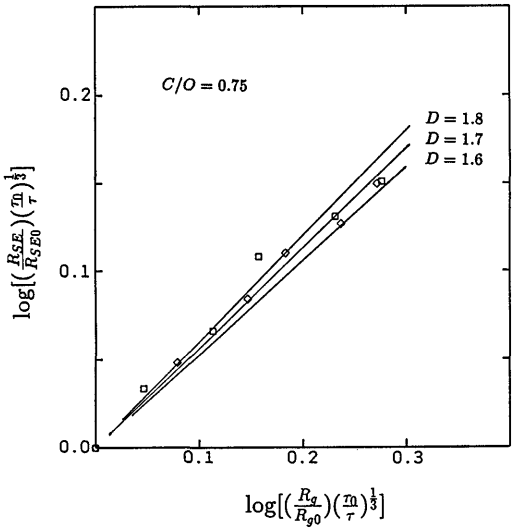

Fig. 3. Plot of data in accordance with Eq. (22) for the C/O = 0.75 flame. Two runs are shown to demonstrate reproducibility. The slope of this plot is $D/3$ to yield a best fit of $D = 1.70 \pm 0.10$. Lines corresponding to $D = 1.60$ and $D = 1.80$ are drawn to illustrate the approximate error in the D measurement.

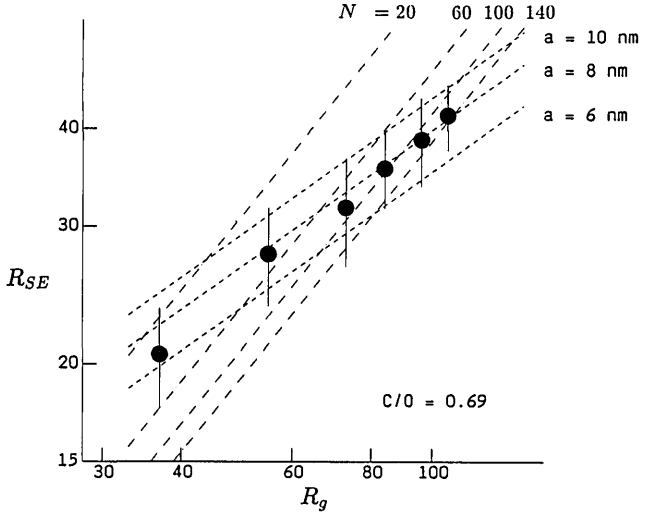

Fig. 4. R_{SE} versus R_g to use the network analysis of Eqs. (19) and (20) for the C/O = 0.69 flame. Lines of constant a and N are drawn. The filled circles represent the precision, determined from reproducibility, of our measurements. The error bars for R_{SE} represent accuracy estimates.

It is now a simple matter to read values of a and N from Figs. 4 and 5 for each flame and height above burner, h. Figure 6 contains the monomer radius a versus h for each flame, and Fig. 7 contains the aggregation number N versus h for each flame. The a values are somewhat smaller but in reasonable accord with values determined from the micrograph inspection of soot aggregates of previous workers.[13,14,27] We find a larger in the sootier C/O = 0.75 flame. In each flame a modest (yet significant because it is greater than the precision uncertainty) increase in a with h is seen, implying the surface deposition of carbon. The N values increase rapidly

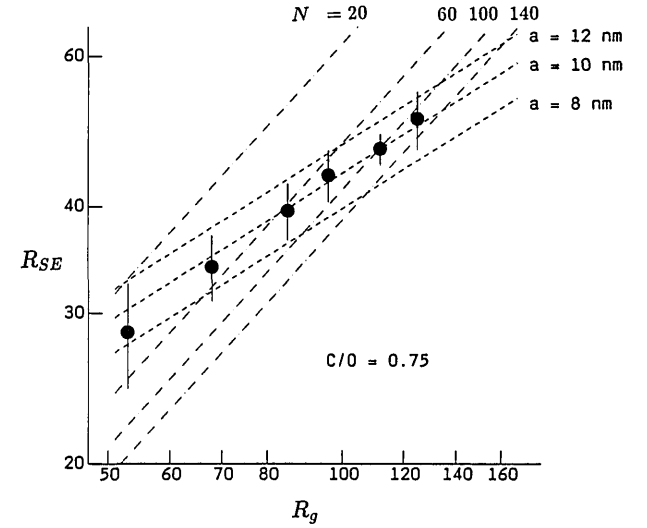

Fig. 5. R_{SE} versus R_g to use the network analysis of Eqs. (19) and (20) for the C/O = 0.75 flame. Lines of constant a and N are drawn. The filled circles represent the precision, determined from reproducibility, of our measurements. The error bars for R_{SE} represent accuracy estimates.

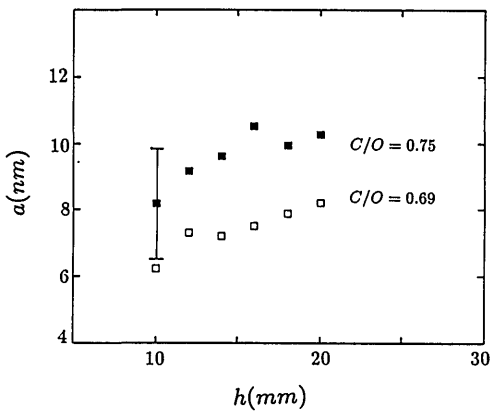

Fig. 6. Monomer radius a under the assumption of a monodisperse size distribution as a function of height above burner h for each flame. A typical error, representing an accuracy estimate propagated from the accuracy of R_{SE}, is given. Correction factors for polydispersity are given in Fig. 8.

with h, as we expected for aggregation. It is interesting to note that N at a given h is roughly the same for each flame. In each case the possibility for valuable kinetics studies awaits future research.

5. Discussion

The purpose of this paper is to demonstrate the feasibility of the in situ optical determination of the monomer radius a and the aggregation number N and a new method for the determination of the fractal dimension D. Section 2 outlined the logic behind our method and our experiment has demonstrated the feasibility on the lowest order. We now sequentially turn to the numerous assumptions we have made to understand their effects on our results.

A. Effects of Polydispersity

The above results are under the assumption that all the clusters have the same aggregation number N, i.e., they are monodisperse. Here we relax this condition and consider the effects of a finite cluster-

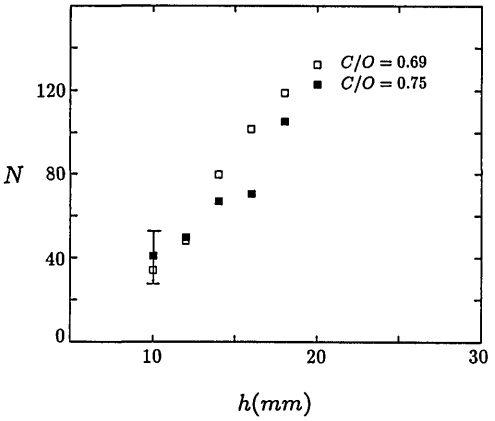

Fig. 7. Number of monomers per cluster N under the assumption of a monodisperse size distribution as a function of height above burner h for each flame. A typical error, representing an accuracy estimate propagated from the accuracy of R_{SE}, is given. Correction factors for polydispersity are given in Fig. 8.

size distribution. We ignore the polydispersity in the monomer radius, which should be significantly smaller than that of N.

Let $n(N)$ be the number of clusters with N monomers per cluster per unit volume per size interval dN. We define the (unnormalized) moments of the distribution as

$$M_i = \int_0^\infty N^i n(N)\mathrm{d}N. \tag{23}$$

For the scattering–extinction measurement, Eqs. (10) and (13) become

$$P_s = I_0 c k^4 a^6 F M_2, \tag{24}$$

$$\tau = 4\pi k a^3 E M_1, \tag{25}$$

hence

$$R_{SE}{}^3 = a^3 M_2/M_1. \tag{26}$$

To find the moments involved in the radius-of-gyration measurement, consider the light scattered by an ensemble of clusters

$$I(q) = \int I(N) n(N)\mathrm{d}N. \tag{27}$$

$I(N)$ is the light scattered by a single N cluster

$$I(N) = N^2 S(qR_g) \tag{28}$$

$$\simeq N^2(1 - \tfrac{1}{3}q^2 R_g{}^2) \tag{29}$$

for $qR_g < 1$. To measure R_g we find the slope of $I(q)/I(0)$ versus q^2. Thus we need

$$\frac{I(q)}{I(0)} = \frac{\int N^2 (1 - \tfrac{1}{3}q^2 R_g{}^2) n(N)\mathrm{d}N}{\int N^2 n(N)\mathrm{d}N}. \tag{30}$$

R_g is converted to N through Eq. (18) and we obtain

$$\frac{I(q)}{I(0)} = 1 - \frac{1}{3} q^2 a^2 k_0{}^{-2/D} \frac{M_{2+2/D}}{M_2}. \tag{31}$$

Thus the measured R_g is related to the moments of the distribution by

$$R_g{}^2 = a^2 k_0{}^{-2/D} \frac{M_{2+2/D}}{M_2}. \tag{32}$$

The ratio of moments in Eqs. (26) and (32) depends on the size distribution, which in turn depends on the coagulation kernel. The coagulation of particles in a flame starts in the kinetic regime. This regime is defined by the Knudsen number, which is the ratio of the gas-molecule mean free path (mfp) to the particle radius, Kn = mfp/r, being significantly greater than one. As the average cluster size grows, the Knudsen number approaches zero and the hydrodynamic or continuum regime of coagulation is entered. In our flames $T \sim 1500$ K, so mfp $\sim$ 330 nm, which implies that the Knudsen number ranges from 20 to 2 as the particles grow from monomers to typical clusters in our flames. Fortunately, both regimes yield self-preserving or scaling size distributions, so the relation between different moments is only a function of the mean size.

To calculate the moments we must know the exact shape of the size distribution. These shapes are somewhat complex for Brownian coagulation. In addition, the shape in the kinetic regime is somewhat different than that in the continuum regime. To simplify our calculations and to yield clean analytic expressions, we use a scaling distribution of the form[23,28]

$$n(N) = M_1 s_1{}^{-2} \phi(N/s_1) = M_1 s_1{}^{-2} \phi(x), \tag{33}$$

where we pick an exponential form for the scaling function

$$\phi(x) = \exp(-x) \tag{34}$$

$$s_1 = M_1/M_0. \tag{35}$$

The moments of the exponential scaling distribution are found to be

$$M_i = M_1 s_1{}^{i-1} \int x^i \phi(x)\mathrm{d}x = M_1 s_1{}^{i-1} \Gamma(i + 1), \tag{36}$$

where Γ is the gamma function. A comparison of the scaling-function moments, $m_i = \int x^i \phi(x)\mathrm{d}x$, calculated from Eq. (36) with those we numerically calculated from the size distribution given by Graham and Robinson[29] is given in Table 1. Graham and Robinson solved the Smoluchowski aggregation equation with a coagulation kernel suitable for coalescence and the kinetic regime, Kn $\gg$ 1. Table 1 shows that the scaling-distribution moments are systematically only $\sim$2% smaller than the exact moments; this is a satisfactory agreement for our purposes here and supports our use of an exponential scaling function. Further support comes from Mulholland *et al.*,[23] who simulated aggregation in the kinetic regime for flame conditions and found their simulated aggregation distribution compared well to a free molecular coales-

Table 1. Comparison of the Scaling Function Moments, $m_i = \int x^i \phi(x)\mathrm{d}x$, of the Self-Preserving Size Distribution

	m_i	
i	Free Molecular[a]	Exponential Scaling
2.25	2.59	2.55
2.50	3.39	3.32
2.75	4.52	4.42
3.00	6.14	6.00
3.25	8.48	8.29
3.50	11.89	11.63
3.75	16.89	16.60
4.00	24.30	24.00

[a]Ref. 29.

cence distribution derived by Lai *et al.*,[30] which is similar to the Graham and Robinson result.

We now use Eq. (36) to evaluate Eqs. (26) and (32) as

$$R_{SE}{}^3 = 2a^3 s_1, \tag{37}$$

$$R_g{}^2 = a^2 k_0{}^{-2/D} s_1{}^{2/D} \frac{\Gamma(3 + 2/D)}{\Gamma(3)}, \tag{38}$$

respectively. Elimination of s_1 between Eqs. (37) and (38) yields

$$R_{SE}{}^3 = a^{3-D} k_0 [2^{1+D/2}/\Gamma(3 + 2/D)]^{D/2} R_g{}^D. \tag{39}$$

Elimination of a between Eqs. (37) and (38) yields

$$R_{SE}{}^3 = k_0{}^{3/D} s_1{}^{1-3/D} 2^{5/2} \Gamma^{-3/2}(3 + 2D) R_g{}^3. \tag{40}$$

These equations are the polydisperse equivalents of Eqs. (19) and (20), which led to the network analysis of constant a and N lines. A comparison to the monodisperse case in Eqs. (19) and (20) leads to the following corrections to be made to the values of a and N determined under the monodisperse assumption:

$$a = [2^{2+D}\Gamma^{-D}(3 + 2/D)]^{1/2(D-3)} a_{\text{mono}} = C_a a_{\text{mono}}, \tag{41}$$

$$s_1 = [\Gamma^3(3 + 2/D)/2^5]^{D/2(D-3)} N_{\text{mono}} = C_N N_{\text{mono}}. \tag{42}$$

Values for these correction factors, C_a and C_N, are plotted in Fig. 8 as a function of D. For our experimental value of $D = 1.73$, we see that the monodisperse values of a determined above plotted in Fig. 6 must be increased by ~ 1.4, whereas the monodisperse values of N plotted in Fig. 7 must be decreased by a factor of ~ 0.18. These corrected values should be considered to be more realistic.

With these corrections the values for R_g plotted in Fig. 1 now appear somewhat too large. Recall, however, that the method we use to measure R_g yields R_g in terms of a ratio of high moments of the size distribution, as shown in Eq. (32). Thus R_g reflects the relative small number of large aggregates at the tail of the distribution (see below).

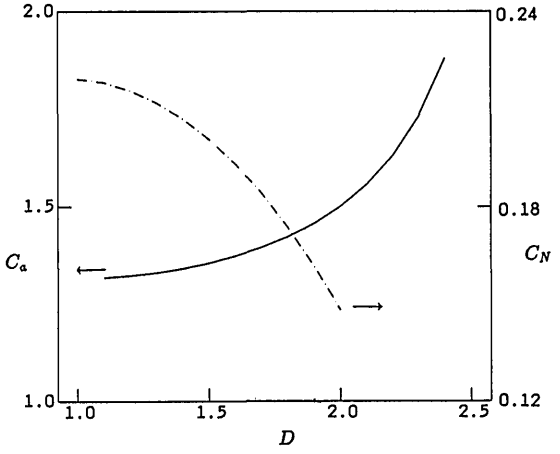

Fig. 8. Correction factors C_a, as shown in Eq. (41), and C_N, as shown in Eq. (42), as a function of the fractal dimension D.

Log-normal (LN) distributions and zeroth-order log-normal distributions (ZOLD) have also been used to describe size distributions of aggregated particles. Geometric widths in the range $\sigma_R \simeq 1.30$ to $\sigma_R \simeq 1.40$ have been found to describe these distributions adequately for coalescing particles such that $D = 3$. In particular, Lee[31] has made analytic solutions of the Smoluchowski equation, which describes aggregation by using a continuum Brownian kernel and an assumed LN to find $\sigma_R = 1.32$ for the self-preserving distribution. One can show that $\sigma_N = \sigma_R{}^D$ where σ_N and σ_R are the geometric widths in N and R space, respectively. Thus $\sigma_N = 1.32^3 = 2.30$ for $D = 3$. The LN and ZOLD yield identical ratios of moments, and these ratios are in reasonable numerical agreement with those obtained from the exponential scaling distribution for $\sigma_N = 2.3$ and $i \leq 2$. In particular, all three distributions predict $M_2/M_1 = 2M_1/M_0$ when $\sigma_N = 2.3$ for any D. This prediction most likely accounts for the success of the ZOLD and LN distributions in describing the self-preserving distribution to some degree of accuracy. This equivalency to scaling is lost, however, for larger moments such as those involved in R_g, $M_{2+2/D}/M_2 \simeq M_3/M_2$. We have seen that the exponential scaling distribution yields moments in good agreement with those obtainable from Graham and Robinson's distribution, as shown in Table 1; in contrast, the LN and ZOLD begin to fail badly for $i > 2$. For this reason we have not used the LN distribution or ZOLD for correcting the monodisperse values of a and N.

B. Variation in Soot-Monomer Number Density

Our method to determine the fractal dimension D, shown in Eq. (22), relied on the assumption that the number of monomers per unit volume was constant in the flame after the reaction zone. At best, this assumption is only half true. We will continue to use the well-founded assumption, with an experimental basis,[32] that the monomers are created solely in the reaction zone and that their number is constant thereafter. Their number density, M_1, however, will vary as the carrier gas volume changes as a result of changes in temperature, flame shape, or gas phase reactions, which change the moles of gas in the flame. We believe that the largest of these effects will be temperature variation and we describe that variation here.

As in the derivation of Eq. (22), we again ratio Eq. (19) at two different points in the flame to eliminate k_0. The values of a are eliminated for τ/M_1 from Eq. (25) to obtain

$$\left(\frac{R_{SE}}{R_{SE,0}}\right)\left(\frac{\tau_0}{\tau}\right)^{1/3}\left(\frac{M_1}{M_{1,0}}\right)^{1/3} = \left[\left(\frac{R_g}{R_{g,0}}\right)\left(\frac{\tau_0}{\tau}\right)^{1/3}\left(\frac{M_1}{M_{1,0}}\right)^{1/3}\right]^{D/3}. \tag{43}$$

Equation (43) replaces Eq. (22) as more general.

The largest variation in M_1 in our flames comes

from temperature variation; M_1 represents the number of monomers per unit volume of flame gas. This gas may be taken as ideal; hence $M_1 \sim T^{-1}$, and $M_1/M_{1,0} = T_0/T$, which may be substituted into Eq. (43).

To describe temperature-variation effects on the D measurement for our flames, we shall look at the extra $M_1/M_{1,0} = T_0/T$ term in Eq. (43) over Eq. (22) as a correction term. This ratio is the same on each side of Eq. (43). Hence the correction would move points in Figs. 2 or 3 along a line of slope unity. Such a line is drawn in Fig. 2 for one of the $h = 20$ mm points. Because the correction line slope is one and the data themselves fall along a line of slope $D/3 \simeq 0.6$, the correction is small. Previous measurements of temperature in another C/O = 0.69 flame on the same burner with nearly the same gas flow rate[33] yielded $T(h = 10\text{ mm}) = 1663$ K, $T(h = 20\text{ mm}) = 1481$ K, and the corrected point is drawn in Fig. 2. The correction is small and will be smaller for other values of h, so we infer that linearity will continue to hold and that it is not necessary for our purpose here to correct all the points. The fractal dimension for the $h = 20$ mm point changes from $D = 1.75$ to $D = 1.81$, which is a +3.5% change. We conclude that this is a reasonable correction to make to our average value of D derived from Figs. 2 and 3 and hence believe a best value of D for our flames is $D = 1.79 \pm 0.10$.

C. Uncertainty in the Soot Index of Refraction

Long the bane of scattering–extinction measurements, the uncertainty of the soot-particle index of refraction propagates into our new analysis for a and N. Whereas R_g is independent of m, R_{SE} is not; hence a and N are affected. The fractal dimension determination is not affected if m is a constant in the flame. This too is an approximation of reality, but the behavior of m as a function of h is not well quantified, so we do not consider this problem here.

From Eq. (14) we see that $R_{SE}{}^3$ is linearly dependent on the factor $E(m)/F(m)$. From Eq. (19), we see that $a \sim R_{SE}{}^{3/(3-D)}$. Hence the relative errors are related as $\mathrm{d}a/a \sim (3 - D)^{-1}\mathrm{d}(E/F)/(E/F)$. For $D = 1.7$, $(3 - D)^{-1} = 0.77$.

Numerous values of m have appeared in the literature, and E/F may be calculated for each. We have calculated E/F for m in the range 1.5–0.5i to 2.0–i and find $0.52 \leq E/F \leq 1.38$, which is a significant variation. Hence these uncertainties can yield considerable uncertainty in a and N. It is ironic that because $R_{SE} \sim (E/F)^{1/3}$, the error to R_{SE} propagated less efficiently (0.33 compared with 0.77) than it does to a and N. This fact was often cited as a reason for not worrying too much about the uncertainty in m when measuring R_{SE}. Now we can make no such rationalization. In contrast, perhaps the sensitivity of a and N to E/F will permit the in situ measurement of this quantity if a and N can be measured independently.

D. Uncertainty in k_0

Whereas considerable effort has been spent demonstrating that the fractal dimension D is a universal quantity, much less attention has been applied to k_0. Our derivation above would imply that k_0 is a function of D and hence universal as well, but it is premature to make such a conclusion. Thus we must be concerned that k_0 may not be what we think it is, as shown in Eq. (21), and ask how uncertainty in k_0 propagates into a and N. From Eqs. (19) and (20), we find $\mathrm{d}a/a \sim (D - 3)^{-1}\mathrm{d}k_0/k_0$ and $\mathrm{d}N/N \sim 3(D - 3)^{-1}\mathrm{d}k_0/k_0$. For $D = 1.7$ these factors are 0.77 and 2.3, respectively. Once again we see that N is the most sensitive. We also note that error in D propagates into k_0 and hence a and N. Fortunately the nature of k_0 means that its uncertainty is a systematic error, not random, and hence does not affect comparisons of a and N at different positions in the flame.

E. Other Considerations

Implicit in all our research above is that the monomers are well-defined spherical particles, and that they touch each other at points. In fact, the contact zones are "necks" thickened to various degrees, and this helps perturb the monomers from pure sphericity. We are uncertain how much this reality affects our idealized calculations. Imagine a fractal of spherical monomers with point contacts. Now thicken this cluster with surface growth. Because the cluster densifies, we expect D to increase as long as thickened cluster can be approximated by a fractal. Our measured D are in reasonable accord with the simulation, despite our measured a's increase of ~30%; so perhaps, we speculate, this effect is not serious. We cannot comment further without theoretically researching this problem.

Next we point out the consistency of our measurements when polydispersity is included and find that this leads us to an important question. For instance, for C/O = 0.69 at $h = 10$ mm, our lowest height above the burner, R_g is roughly twice as large as R_{SE}, and R_{SE} in turn is a little more than twice as big as a when corrected for polydispersity. From Fig. 7, $N_{\mathrm{mono}} \simeq 36$, which when corrected by Eq. (42) using Fig. 8 yields $s_1 \simeq 6$. Now R_{SE} determined from the ratio of scattering to extinction is given by $R_{SE} = as_2{}^{1/3}$. Because $s_2 = 2s_1 \simeq 12$, we find $R_{SE}/a \simeq 2.3$, which is correct. Furthermore, $(R_g/a)^D$ goes approximately as $s_3 = 3s_1 \simeq 18$, so $R_g/a \simeq 5.2$ is again consistent with our observation.

The example above leads us to confront the question: as N decreases, when does a fractal cluster stop being a fractal? Or, when do Eqs. (7) and (8) for fractal optics cease to apply? We ask these questions because s_1 is only $\simeq 6$. Graphs for simulated particles of R_g versus N show the power-law behavior of relation (1) to $N = 10$ and below. We used this fact, i.e., the $N \to 1$ limit, to derive the value of k_0 in Eq. (21) and this value agreed to some reasonable degree with simulations. For optics we know R_g values are

independent of fractal concepts. Also, light scattering sees the large end of the distribution. The relevant moment ratio for R_{SE} is $s_2 = 2s_1$ and for R_g is approximately $s_3 = 3s_1$. Hence s_1 may be only 6, but s_2 is 12 and s_3 is 18. We also remember that light scattering forms an ensemble average of all the clusters in the scattering volume. Perhaps any single small N cluster is not well described by fractal morphology and optics, but the average of an ensemble of them is. Fortunately, the rest of our measurements are for larger clusters, where the small N limit is not a problem. Certainly we cannot ignore the consistency of our results and the reasonable values we have obtained for D, a, and $N(s_1)$; therefore it seems that our procedure is working correctly. For future research with smaller clusters, it would be valuable to have a theoretical comparison of exact small-cluster optics to the fractal optics used in this paper.

6. Conclusions

We have shown that the combination of two static light-scattering techniques that measure either amount of material or ramified size can together yield the detailed structural information for the mean aggregate, i.e., the monomer size a, the number of monomers per aggregate N, and the fractal dimension D. The *in situ* determination of a and N represents a significant advance in our measurement abilities. Our method to measure D is new and of value not only for comparison with structure-factor measurements that can yield D, but also for use when qR_g is small and structure-factor measurements are inaccurate. Determination of other quantities such as the number of aggregates per unit volume and volume fraction of soot have not been discussed here, but their determination follows in a straightforward manner from the fundamental relations above.

Our analysis has shown a large accuracy uncertainty in the measured values of a and N. Whether this uncertainty is important or not is dependent on the application. The combination of a or N into cluster number density or volume fraction leads to compensating errors; hence these latter values are well determined. The precision as determined by run-to-run consistency of a and N is, in contrast, quite good. This is fortunate, for the analysis of kinetic processes in flames will rely on changes of a and N, which are affected by precision, not accuracy. Thus the future application of the optical techniques developed here to understanding flame kinetics should be secure.

This research was supported by the National Science Foundation and the National Institute for Standards and Technology through grant CTS-9024668.

References

1. A. D'Alessio, A. DiLorenzo, A. F. Sarofim, F. Beretta, S. Masi, and C. Venitozzi, "Soot formation in methane-oxygen flames," in *Fifteenth Symposium (International) on Combustion* (Combustion Institute, Pittsburgh, Pa., 1975), p. 1427.
2. A. D'Alessio, "Laser light scattering and fluorescence diagnostics of rich flames," in *Particulate Carbon*, D. C. Siegla and G. W. Smith, eds. (Plenum, New York, 1981), p. 207.
3. W. Hinds and P. C. Reist, "Aerosol measurement by laser Doppler spectroscopy," Aerosol Sci. **3,** 501–514, 515–529 (1982).
4. G. B. King, C. M. Sorensen, T. W. Lester, and J. F. Merklin, "Photon correlation spectroscopy used as a particle size diagnostic in sooting flames," Appl. Opt. **21,** 976–978 (1982).
5. S. M. Scrivner, T. W. Taylor, C. M. Sorensen, and J. F. Merklin, "Soot particles size distribution measurements in a premixed flame using photon correlation spectroscopy," Appl. Opt. **25,** 291–297 (1986).
6. W. L. Flower, "Optical measurements of soot formation in flames," Combust. Sci. Technol. **33,** 17–33 (1983).
7. M. E. Weill, P. Flament, and G. Gousebet, "Diameters and number densities of soot particles in premixed flat flames, propane/oxygen," Appl. Opt. **22,** 2407–2409 (1983).
8. M. E. Weill, N. Lhuissier, and G. Gouesbet, "Mean diameters and number densities of soot particles in premixed flat flames CH_4-O_2 by diffusion broadening spectroscopy," Appl. Opt. **25,** 1676–1683 (1986).
9. S. R. Forrest and T. A. Witten, "Long-range correlations in smoke-particle aggregates," J. Phys. A **12,** L109–L117 (1979).
10. F. Family and D. P. Landau, eds., *Kinetics of Aggregation and Gelation* (North-Holland, Amsterdam, 1984).
11. H. E. Stanley and N. Ostrowsky, eds., *On Growth and Form* (Nijhoff, Boston, Mass., 1986).
12. B. Mandelbrot, *The Fractal Geometry of Nature* (Freeman, San Francisco, Calif., 1983).
13. R. J. Samson, G. W. Mulholland, and J. W. Gentry, "Structural analysis of soot agglomerates," Langmuir **3,** 273–281 (1987).
14. R. A. Dobbins and C. M. Megaridis, "Morphology of flame-generated soot as determined by thermophoretic sampling," Langmuir **3,** 254–259 (1987).
15. T. Freltoft, J. K. Kjems, and S. K. Sinha, "Power-law correlations and finite-size effects in silica particle aggregates studied by small-angle neutron scattering," Phys. Rev. B **33,** 269–275 (1986).
16. R. D. Mountain and G. W. Mulholland, "Light scattering from simulated smoke agglomerates," Langmuir **4,** 1321–1326 (1988).
17. M. V. Berry and I. C. Percival, "Optics of fractal clusters such as smoke," Opt. Acta **33,** 577–591 (1986).
18. J. Nelson, "Test of a mean field theory for the optics of fractal clusters," J. Mod. Opt. **36,** 1031–1057 (1989).
19. A. J. Hurd and W. L. Flower, "In situ growth and structure of fractal silica aggregates in a flame," J. Colloid Interface Sci. **122,** 178–192 (1988).
20. H. X. Zhang, C. M. Sorensen, E. R. Ramer, B. J. Olivier, and J. F. Merklin, *"In-situ* optical structure factor measurements of an aggregating soot aerosol," Langmuir **4,** 867–871 (1988).
21. S. Gangopadhyay, I. Elminyawi, and C. M. Sorensen, "Optical structure factor measurements of soot particles in a premixed flame," Appl. Opt. **25,** 4859–4864 (1991).
22. M. Kerker, *The Scattering of Light and Other Electromagnetic Radiation* (Academic, New York, 1969).
23. G. W. Mulholland, R. J. Samson, R. D. Mountain, and M. H. Ernst, "Cluster size distribution for free molecular aggregation," J. Energy Fuels **2,** 481–486 (1988).
24. S. J. Harris and A. M. Weiner, "Surface growth of soot particles in premixed ethylene/air flames," Combust. Sci. Technol. **31,** 155–167 (1983).
25. S. J. Harris and A. M. Weiner, "Determination of the rate constant for soot surface growth," Combust. Sci. Technol. **32,** 267–275 (1983).

26. W. H. Dalzell and A. F. Sarofim, "Optical constants of soot and their application to heat-flux calculations," J. Heat Transfer **91,** 100–104 (1969).
27. J. Lahaye and G. Prado, "Morphology and internal structure of carbon blacks and soot," in *Particulate Carbon,* D. C. Siegla and G. W. Smith, eds. (Plenum, New York, 1981), p. 33.
28. P. G. van Dongen and M. H. Ernst, "Dynamic scaling in the kinetics of clustering," Phys. Rev. Lett. **54,** 1396–1394 (1985).
29. S. C. Graham and A. Robinson, "A comparison of numerical solutions to the self-preserving size distribution for aerosol coagulation in the free-molecular regime," J. Aerosol Sci. **7,** 261–273 (1976).
30. F. S. Lai, S. K. Friedlander, J. Pich, and G. M. Hidy, "The self-preserving particle size distribution for Brownian coagulation in the free-molecule regime," J. Colloid Interface Sci. **39,** 395–405 (1972).
31. K. W. Lee, "Change of particle size distribution during Brownian coagulation," J. Colloid Interface Sci. **92,** 315–325 (1983).
32. C. M. Megaridis and R. A. Dobbins, "Comparison of soot growth and oxidation in smoking and non-smoking ethylene diffusion flames," Combust. Sci. Technol. **66,** 1–16 (1989).
33. E. R. Ramer, J. F. Merklin, and C. M. Sorensen, "The effect of benzene doping on the sootiness of a premixed methane-oxygen flame," Combust. Sci. Technol. (to be published).